

A Parametric Level Set Method for Electrical Impedance Tomography

Dong Liu¹, Anil Kumar Khambampati, and Jiangfeng Du

Abstract—This paper presents an image reconstruction method based on parametric level set (PLS) method using electrical impedance tomography. The conductivity to be reconstructed was assumed to be piecewise constant and the geometry of the anomaly was represented by a shape-based PLS function, which we represent using Gaussian radial basis functions (GRBF). The representation of the PLS function significantly reduces the number of unknowns, and circumvents many difficulties that are associated with traditional level set (TLS) methods, such as regularization, re-initialization and use of signed distance function. PLS reconstruction results shown in this article are some of the first ones using experimental EIT data. The performance of the PLS method was tested with water tank data for two-phase visualization and with simulations which demonstrate the most popular biomedical application of EIT: lung imaging. In addition, robustness studies of the PLS method w.r.t width of the Gaussian function and GRBF centers were performed on simulated lung imaging data. The experimental and simulation results show that PLS method has significant improvement in image quality compared with the TLS reconstruction.

Index Terms—Electrical impedance tomography, parametric level set method, lung imaging, inverse problems.

I. INTRODUCTION

ELECTRICAL impedance tomography (EIT) is an imaging modality that aims to recover the spatially distributed conductivity inside the interested object from the surface electrical measurements. Being a safe (non-radiation), non-intrusive, and inexpensive methodology, it has proven to

Manuscript received August 18, 2017; revised September 15, 2017; accepted September 20, 2017. Date of publication September 26, 2017; date of current version February 1, 2018. This work was supported in part by the 973 Program of China under Grant 2013CB921800, in part by the National Natural Science Foundation of China under Grant 11227901, in part by the CAS under Grant XDB01030400 and Grant QYZDY-SSW-SLH004, and in part by the Anhui Provincial Natural Science foundation under Grant 1708085MA25 (Corresponding authors: Dong Liu; Jiangfeng Du.)

D. Liu and J. Du are with the CAS Key Laboratory of Microscale Magnetic Resonance and Department of Modern Physics, University of Science and Technology of China, Hefei 230026, China, and also with Hefei National Laboratory for Physical Sciences at the Microscale, University of Science and Technology of China, Hefei 230026, China, and also with the Synergetic Innovation Center of Quantum Information and Quantum Physics, University of Science and Technology of China, Hefei 230026, China (e-mail: (dong.liu@outlook.com; djf@ustc.edu.cn).

A. K. Khambampati is with the BK21+ Clean Energy Convergence and Integration Center for Human Resources Training and Education, Jeju National University, Jeju 63243, South Korea.

Color versions of one or more of the figures in this paper are available online at <http://ieeexplore.ieee.org>.

Digital Object Identifier 10.1109/TMI.2017.2756078

be useful in a number of industrial [1], [2] and medical applications. Medical applications include monitoring of lung function [3]–[5], detection of breast cancer [6] and imaging of brain activity [7].

The image reconstruction of EIT is a nonlinear *ill-posed* inverse problem. Therefore, the reconstruction approaches in EIT need to be regularized to overcome the extreme sensitivity to measurement noise and modeling errors [8]–[10]. For example, based on *a priori* knowledge about the unknowns (e.g., conductivity), the inverse problem is subjected to constraints that make use of various regularization schemes to stabilize the reconstructions. Traditionally, regularization methods such as Tikhonov and total variation have been employed and the regularization parameter is determined heuristically or selected automatically using L-curve method [11], [12]. Generally speaking, these regularization schemes are employed in situations where one aims to use the EIT measurements to recover the conductivity distributions associated with a dense discretization of the interested object (e.g., pixels or voxels).

In addition, the EIT reconstruction problem can also be solved by incorporating structural prior information [13], employing special designed basis functions [14], and reducing dimensionality of the problem for improving the condition number of inverse problem.

In many applications of EIT, including medical imaging, it is important to identify and characterize regions-of-interest in the object (for example, tumors in the breast [6], air content in the local lung [15], cracks in a concrete samples [16] etc). For such problems, an alternative to estimation of conductivity distribution and then post-processing to identify the region is to use the geometric inversion methods to directly recover the information regarding hidden anomalies. Problems tackled in this way are known as the shape-based problems. For earlier works arising from EIT, see [17]–[20] for example. Such processes usually involve reformulating the problem of the conductivity reconstruction as an inverse problem for a special geometrical representation of embedded objects, by using a level set function (LSF).

The idea of level set was initially proposed in [21] for tracking propagating interfaces through topological changes and more recently it has also found applications in shape reconstruction problems [17]–[20], [22]–[24] and in inverse scattering problems [25]. Compared to the more commonly used pixel/voxel-based reconstruction methods, the advantage of shape-based level set method (LSM) is threefold:

First, LSM employs priors of conductivity explicitly in the modeling of the problem, allowing a chance to achieve high contrast reconstructed image, and second, the use of a LSF (which is an implicit representation of the shapes) frees us from topological restrictions during the reconstruction, providing a method to automatically trace the topology changes of geometries such as shape splitting/emerging and holes developing. Finally, LSM is applicable in two and three dimensions. In general, many different approaches for the shape reconstruction are possible in two dimensions, but their extension to three dimensions is notoriously difficult. For example, spline-based method has been applied to estimate shape and free surface in EIT [26].

Although the traditional level set (TLS) method provides large degrees of flexibility in shape reconstruction, there are numerical concerns associated with this method. It has been found that the LSF could be changed into a non-distance function with the initial LSF defined as a signed distance function [27], [28]. This causes some applications to fail, such as image segmentation [29]. It is, therefore, necessary to correct or re-initialize the LSF to keep it well behaved, which is usually inevitable and add extra computational costs and complexity to the problem [30]. Moreover, in TLS methods, the unknown LSF belongs to an infinite dimensional function space. From an implementation perspective, this requires the discretization of the LSF onto a dense mesh, which tends to be time consuming. Such problems in TLS motivated us to consider a geometric inversion method based on a low order parametric model, which has been shown to perform well in the context of ill-posed inverse problems [31].

In this paper, inspired from works [24], [31], we consider the use of a shape-based approach to EIT based on a parametric level set (PLS) formulation. In the proposed PLS approach, the conductivity to be reconstructed was assumed to be piecewise constant and the geometry of the anomaly was represented by a shape-based PLS function, which we represent using Gaussian radial basis functions (GRBF). A key point in PLS method is to provide a low order representation of the LSF. This representation of the LSF not only decreases the number of unknowns and therefore the computational cost of the inversion, but also tends to improve the condition number of the inverse problem compared to pixel/voxel-based image reconstruction and TLS reconstruction. Another advantage of PLS method is that it does not intrinsically require reinitialization of the LSF as in TLS, since the LSF is more likely to remain well behaved through the aforementioned representation in PLS.

We note that electrical resistance tomography (ERT, which is a particular case of EIT) has been studied in the work [31] as an illustrative example. In that study, a point electrode model was used for formulating the forward problem of EIT. However, the point electrode model is not an accurate model when considering real applications, e.g., it does not take impedances of electrodes into account [32]. Conventionally, the most accurate physically realizable model in EIT is the complete electrode model (CEM) [33], which has been shown to have a unique solution and predict the experimental measurements accurately [34]. Further, to our best knowledge,

there is no studies of PLS with EIT experimental data, as well as considering potential medical application in EIT. In this paper, we applied the PLS method into EIT and solved the forward problem with CEM.

To evaluate the accuracy of PLS method, we use experimental data to show the improvement of the PLS method over the pixel based TLS method. Simulation data are used to show PLS reconstructions for EIT lung imaging. In addition, simulation data are also used to study the robustness of PLS method *w.r.t* width of Gaussian radial basis function by varying the number of basis functions and their center locations. Moreover, performance of PLS method is studied with and without modeling error due to non-homogeneous background.

The rest of this paper is structured as follows. In Section II, we briefly review the EIT forward model. In Section III we discuss the PLS method and in Section IV we present experimental results that show the improvement of the PLS method over pixel-based methods. The PLS method and its robustness studies are tested with simulations related to lung imaging application in Section V. Finally, the conclusions are drawn in Section VI.

II. EIT FORWARD PROBLEM

Let us denote the body under investigation by $\Omega \subset \mathbb{R}^q$, $q = 2, 3$, and its boundary by $\partial\Omega$. The electric potential $u(x)$ inside Ω induced by the injected current I_ℓ can be modeled using the CEM [34]

$$\nabla \cdot (\sigma(x)\nabla u(x)) = 0, \quad x \in \Omega, \quad (1)$$

$$u(x) + z_\ell \sigma(x) \frac{\partial u(x)}{\partial n} = U_\ell, \quad x \in e_\ell, \quad \ell = 1, \dots, L \quad (2)$$

$$\int_{e_\ell} \sigma(x) \frac{\partial u(x)}{\partial n} dS = I_\ell, \quad \ell = 1, \dots, L \quad (3)$$

$$\sigma(x) \frac{\partial u(x)}{\partial n} = 0, \quad x \in \partial\Omega \setminus \bigcup_{\ell=1}^L e_\ell \quad (4)$$

where $\sigma(x)$ is the conductivity, $x \in \Omega$ is the spatial coordinate, z_ℓ is the contact impedance between electrodes and the imaged body; U_ℓ and I_ℓ denote the potential and current corresponding to electrode e_ℓ , respectively; L denotes the number of electrodes and n denotes an outward unit normal.

In addition, the charge conservation condition

$$\sum_{\ell=1}^L I_\ell = 0, \quad (5)$$

needs to be fulfilled. Further, to determine uniquely the potentials u and U based on the CEM, the potential reference level needs to be fixed, e.g.,

$$\sum_{\ell=1}^L U_\ell = 0. \quad (6)$$

By numerically approximating the CEM (1-6), e.g., using *finite element method* (FEM) [35], the observation model can be written in the form

$$V = U(\sigma) + e, \quad (7)$$

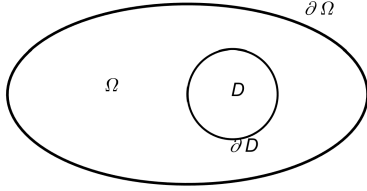


Fig. 1. Illustration of object and region of interest used for parametric level set method.

where V is a collection of all the measured voltages, $U(\sigma)$ is the FEM solution to the forward problem, and e is additive Gaussian noise with mean e^* and covariance matrix Γ_e .

III. SHAPE RECONSTRUCTION USING PARAMETRIC LEVEL SET METHOD

In this section, the PLS method which is used for solving the EIT reconstruction problem is introduced. For simplicity of presentation, we assume the domain Ω contains two different regions D and $\Omega \setminus D$ with piecewise constant conductivity distribution as $\sigma(x) = \sigma_1$ for $x \in D$ and $\sigma(x) = \sigma_0$ for $x \in \Omega \setminus D$, as shown in Fig.1.

In association with the two regions represented by one LSF $f(x)$, the interior conductivity distribution $\sigma(x)$ in Ω is described as follows

$$\sigma(x) = \sigma_0(1 - H(f(x))) + \sigma_1(H(f(x))) \quad (8)$$

where $H(s)$ is the Heaviside function, defined as

$$H(s) = \begin{cases} 1 & \text{for } s \geq 0, \\ 0 & \text{for } s < 0, \end{cases} \quad (9)$$

and $f(x)$ is the LSF satisfying

$$\begin{cases} f(x) > 0 & \forall x \in D, \\ f(x) = 0 & \forall x \in \partial D, \\ f(x) < 0 & \forall x \in \Omega \setminus D. \end{cases} \quad (10)$$

In practice, we use a smooth version of the Heaviside function [36], [37] denoted as $H_\varepsilon(s)$ where $H_\varepsilon(s)$ is computed as

$$H_\varepsilon(s) = \begin{cases} 1 & s > \varepsilon, \\ 0 & s < -\varepsilon, \\ \frac{1}{2} \left[1 + \frac{s}{\varepsilon} + \frac{1}{\pi} \sin\left(\frac{\pi s}{\varepsilon}\right) \right] & |s| \leq \varepsilon. \end{cases} \quad (11)$$

Here, the parameter ε defines a band $\mathcal{S}_b = 2\varepsilon$ within which the Heaviside function is smoothed [37].

As discussed in Section I, we represent the LSF $f(x)$ parametrically, so instead of using a signed distance function in TLS method [19], it is represented using radial basis functions (RBFs)

$$f(x) = \sum_{i=1}^N \mu_i p_i(x), \quad (12)$$

where $\mu = [\mu_1, \mu_2, \dots, \mu_N] \in \mathbb{R}^N$ is the PLS parameter vector whereas $p_i(x)$ are the functions which belong to the basis set of $P = \{p_1, p_2, \dots, p_N\}$, where N denotes the

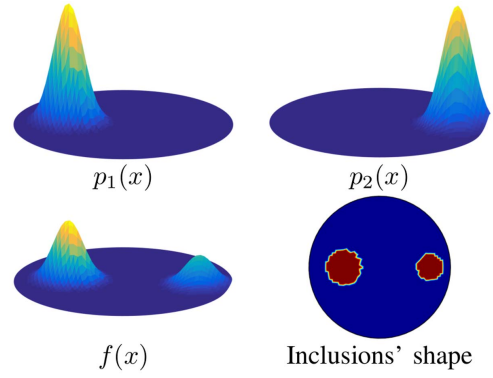


Fig. 2. Illustration of representing LSF in PLS method. $p_1(x)$ and $p_2(x)$ are the GRBFs, $f(x) = \frac{1}{2}p_1(x) + \frac{1}{4}p_2(x)$ is the LSF and the shape of inclusions is obtained by taking the contour of $f = 0.1$ level set.

number of the basis functions $p_i(x)$. Possible choices for the P basis set include Gaussian, multiquadric, polyharmonic splines and thin plate splines polynomial. For the purpose of this paper, we use Gaussian radial basis function (GRBF). That is,

$$p_i(x) = \exp\left(-\frac{\|x - x_i\|^2}{2\gamma^2}\right), \quad (13)$$

where γ is the Gaussian width and $\|\cdot\|$ denotes the Euclidean norm. This representation of LSF in PLS is illustrated in Fig. 2.

Based on the parameterization of the LSF, equation (10) can be modified as

$$\begin{cases} f(x, \mu) > c & \forall x \in D, \\ f(x, \mu) = c & \forall x \in \partial D, \\ f(x, \mu) < c & \forall x \in \Omega \setminus D, \end{cases} \quad (14)$$

here, c is a small positive value.

Based on equation (14), the conductivity distribution in (8) can be expressed as

$$\sigma(x, \mu) = \sigma_0(1 - H(f(x, \mu) - c)) + \sigma_1(H(f(x, \mu) - c)). \quad (15)$$

Unlike the conductivity model in (8) of TLS method that maps the space of unknown regions D into the unknown LSF $f(x)$, this model in fact maps the space of unknown regions D into the space of unknown PLS parameter μ , reducing significantly the number of unknowns.

Now the observation model in (7) can be expressed as

$$V = U(\sigma(x, \mu)) + e. \quad (16)$$

Then, the shape reconstruction and estimation of piecewise constant values σ_0 and σ_1 in PLS amounts to solving the minimization problem

$$[\hat{\mu}, \hat{\sigma}_0, \hat{\sigma}_1] = \arg \min \{ \|L_e(V - U(\sigma))\|^2 + \|I(\mu - \mu^*)\|^2 + \sum_{j=0}^1 \|I(\sigma_j - \sigma_j^*)\|^2 \}. \quad (17)$$

Here L_e is defined as $L_e^T L_e = C_e^{-1}$, where C_e is the observation noise covariance matrix, I is the identity matrix.

μ^* and σ_j^* are predetermined constant values (see Sections IV-B and IV-C). The last two terms on the right-hand side of (17) is referred to as the penalty terms, allowing to obtain stable reconstructions with faster converging speed.

We note that in the minimization problem (17), unknown σ_0 and σ_1 are appended to the unknown PLS parameter μ , and are estimated together with μ simultaneously. For some special cases, the binary conductivity values σ_0 and σ_1 are known *a priori*, then the shape reconstruction in PLS method can be simplified to minimize the first two terms of the right-hand side of (17). We refer to the solution of this special case as shape-only reconstruction with PLS method.

Similarly as in [38], the solution of (17) has to be computed iteratively. In the iterations, the Jacobian matrix $J_U(\mu, \sigma_0, \sigma_1) = \frac{\partial U}{\partial(\mu, \sigma_0, \sigma_1)}$ is needed. To begin, taking a derivative of σ w.r.t f yields

$$\frac{\partial \sigma}{\partial f} = (\sigma_1 - \sigma_0)(\delta(f - c)), \quad (18)$$

where $\delta(\cdot)$ denotes the Dirac delta function. Based on the observation model (16), the derivative of the calculated voltage U w.r.t the PLS parameter μ_i can be split into a product of three partial derivatives yielding

$$J_U(\mu) = \frac{\partial U}{\partial \sigma} \cdot \frac{\partial \sigma}{\partial f} \cdot \frac{\partial f}{\partial \mu} = J_U(\sigma)(\sigma_1 - \sigma_0)(\delta(f - c)) \frac{\partial f}{\partial \mu}, \quad (19)$$

where $J_U(\sigma)$ can be computed with the standard method, see details in [11]. In a similar way, we can get

$$J_U(\sigma_0) = \frac{\partial U}{\partial \sigma} \cdot \frac{\partial \sigma}{\partial \sigma_0} = J_U(\sigma)(1 - H(f - c)), \quad (20)$$

and

$$J_U(\sigma_1) = \frac{\partial U}{\partial \sigma} \cdot \frac{\partial \sigma}{\partial \sigma_1} = J_U(\sigma)(H(f - c)). \quad (21)$$

Finally, the minimization problem in (17) is iteratively solved by using the Gauss-Newton method with a line search, and the positivity constraint on the conductivity is handled by using interior point methods.

IV. EXPERIMENTAL STUDIES

The feasibility of the proposed PLS method was evaluated experimentally with tank data corresponding to different conductivities. All tests, marked as Cases 1-7, were carried out with inclusions that were homogeneous in the vertical direction and extended through the water surface, and hence two-dimensional models were adequate for modeling the measurements. The extension of the computational methods to a purely three-dimensional case is straightforward.

A. Experimental Setup

In the experiments, a cylindrical tank was filled with saline of conductivity $543 \mu\text{s}/\text{cm}$, and seven different target conductivities were constructed by inserting non-conductive (plastic objects in Cases 1-6) and conductive inclusions (pumpkin and rutabaga in Case 7) with different shapes into the tank.

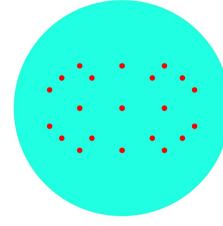


Fig. 3. Distributions of the RBF centers x_i used for the PLS method in the experimental studies.

Photos of all six high-contrast (Cases 1-6) and one low-contrast experiments (Case 7) are shown in the left column of Figs. 4 & 5. The diameter of the tank was 28 cm. Sixteen equally spaced metallic electrodes (width 2.5 cm, height 7.0 cm) were attached to the inner surface of the tank. The experiments were carried out using with KIT4 measurement system [39]. In the EIT measurements, the amplitude of the injected current was 1 mA and the frequency was set to 10 kHz. Four electrodes $\{i = 1, 5, 9, 13\}$ were selected as sink electrodes, and pairwise current injections between electrode pairs i and j , $j = 1, \dots, 16$, $i \neq j$ were applied, leading to total of 54 injections when reciprocal injections were removed. Corresponding to each current injection, the potentials of all 15 electrodes were measured against the sink electrode, which was connected to the common ground, i.e., the ground level in (6) holds.

B. Implementation Issues

In the PLS reconstructions, the GRBFs was calculated in a piece-wise linear 1st order nodal FE basis with $N_n = 3613$ nodes, and the voltage was approximated in the 2nd order basis with $N_n = 14209$ nodes and $N_e = 6984$ elements. Note that the element information is same for both the 1st and 2nd order basis.

Before describing how to select the Gaussian width parameter γ for the GRBF in the PLS reconstruction, we rewrite the GRBF (13) in the new form of

$$p_i(x) = \exp(-\lambda \|x - x_i\|^2). \quad (22)$$

Then,

$$\gamma = \frac{1}{\sqrt{2\lambda}}. \quad (23)$$

It is apparent that adjusting the parameter variant λ has the same significance as adjusting the width γ of GRBF. Let \mathcal{A} denote the mean value of the element area in the FEM mesh, namely, $\mathcal{A} = \frac{\text{Tank area}}{N_e} = 0.0882$ for the FEM mesh mentioned above. The PLS reconstruction process is initialized with $N = 21$ GRBFs with width parameter variant

$$\lambda = \mathcal{K}\mathcal{A}, \quad (24)$$

placed randomly on the FEM grid in the domain to be imaged. Here, \mathcal{K} is a free coefficient of the Gaussian width parameter, which we heuristically set $\mathcal{K} = 2$ for the experimental studies. Thus, the unknown parameters vector $(\mu, \sigma_0, \sigma_1)^T \in \mathbb{R}^{23}$. A representative image of the distribution of the RBF centers x_i is shown in Fig.3.

TABLE I
THE RELATIVE SIZE COVERAGE RATIOS (RCRs) OF
THE RECOVERED INCLUSIONS

	Case 1	Case 2	Case 3	Case 4	Case 5	Case 6	Case 7
True	1.00	1.00	1.00	1.00	1.00	1.00	1.00
PLS	1.03	1.04	0.97	1.04	1.01	0.91	1.09
TLS	0.84	0.90	1.00	0.98	0.82	0.84	1.51

For all studies presented in this paper, the μ'_i 's weight coefficients were initialized to 0.5. For the shape representation Heaviside function (11) with $\varepsilon = \mathcal{A}/2$ was used and the constant $c = f_m$ level set is considered, where f_m is the mean value of the initial LSF f . Note that the same parameter selection was used in all studies.

In addition, the PLS method presented here is compared with the TLS method using a typical Gauss-Newton approach with the LSF defined as a signed distance function over the pixels and a smoothness regularization added. Based on (7) and (8), the reconstruction of TLS method is obtained by solving the minimization problem:

$$[\hat{f}, \hat{\sigma}_0, \hat{\sigma}_1] = \arg \min \{ \|L_e(V - U(\sigma))\|^2 + \|L_f(f - f^*)\|^2 + \sum_{j=0}^1 \|I(\sigma_j - \sigma_j^*)\|^2 \}, \quad (25)$$

where f^* is the initial LSF, calculated as the signed distance function from a given initial circle of radius 5 centered at $(-5, 1)$, and $L_f^T L_f = \Gamma_f^{-1}$, and Γ_f for the LSF consists of the entries (see e.g., [40])

$$\Gamma_f(j, k) = a \exp \left\{ -\frac{\|x_j - x_k\|_2^2}{2b^2} \right\} + d\delta_{jk}, \quad (26)$$

where $x_j, x_k \in \Omega$ are the coordinates of the mesh nodes corresponding to LSF value f_j and f_k , respectively; a, b and d are positive scalar parameters, and δ_{jk} denotes the Kronecker delta function. With this construction, the variation of LSF is $a+d$, we set $a = 10$ and $d = 0.001$ (which is used to ensure that Γ_f is well-conditioned). Parameter b controls the degree of spatial smoothness, which is set to 1. These parameters were experimentally selected so that the reconstructions are visually acceptable. For the Bayesian interpretation of the parameters in (26), see [41].

C. Experimental Results and Analysis

The results are shown in Figs. 4 & 5 using the same color scale from 0 to 0.57. The first column of Figs. 4 & 5 shows the true targets; The second column shows the shape reconstruction using the PLS method; The last column shows the result of the same problem using the TLS method.

For quantitating the results, we computed the relative size coverage ratio (RCR), shown in Table I for the inclusions in the reconstructed images:

$$\text{RCR} = \frac{\text{CR}}{\text{CR}_{\text{True}}}, \quad (27)$$

where CR denotes the coverage ratio defined as the ratio of the size of the inclusions to the total size of the target. Correspondingly, CR_{True} is the CR of the true target. Value 1

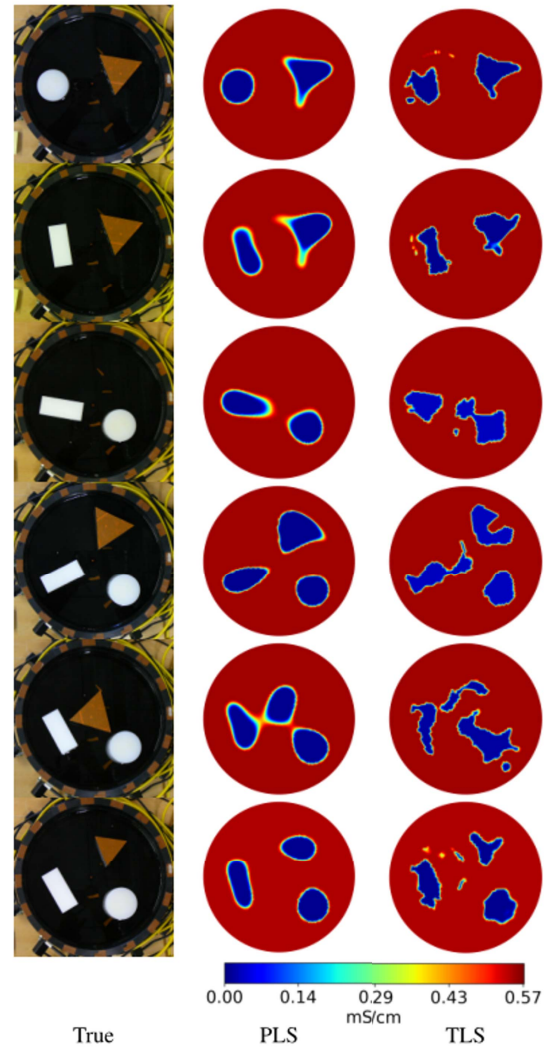


Fig. 4. Reconstructions of the *high-contrast* experiments with both PLS and TLS methods. Inclusions are composed of plastic objects. Cases 1-6 are shown from top to bottom.

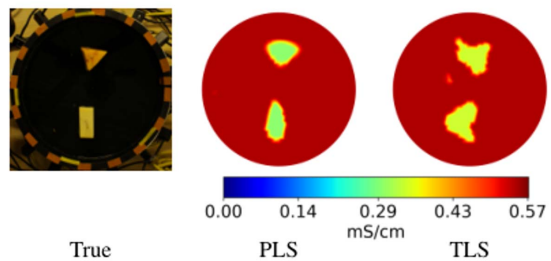


Fig. 5. Case 7: Reconstructions of the *low-contrast* experiment with both PLS and TLS methods. Inclusions are composed of pumpkin and rutabaga.

would indicate exact match of size of the true and recovered inclusions, while a value greater or less than 1 would indicate overestimation or underestimation, respectively.

In both methods, the piecewise constant σ_0 and σ_1 are estimated together with the shape estimation, giving reasonable estimation for all the cases. For example, in the fifth row's target (case 5), the initial values used for the conductivity values are $\sigma_0 = 0.4144$ mS/cm and $\sigma_1 = 0.0014$ mS/cm. The initial guess of the background conductivity $\sigma_0 \in \mathbb{R}$ and

contact impedance $z \in \mathbb{R}$ were computed by solving

$$[\hat{\sigma}_0, \hat{z}] = \arg \min \{ \|L_e(V - U(\sigma_0, z))\|^2 \}. \quad (28)$$

Note that the measurements with a homogenous target are not a necessity for the reconstruction. The final resulting values $\sigma_0 = 0.5489$ mS/cm and $\sigma_1 = 7.1 \times 10^{-5}$ mS/cm with PLS method, $\sigma_0 = 0.5520$ mS/cm and $\sigma_1 = 0.0178$ mS/cm with TLS method, demonstrates that the PLS reconstructions have a better match with real quantities (the plastic inclusions are almost non-conductive and the measured saline conductivity is 0.543 mS/cm).

As the results in Fig. 4 show, both corresponding to TLS and PLS methods, the inclusions are clearly visible, and the positions of the inclusions correspond to the real targets. In all test cases, the PLS methods performs well in reconstructing major shape characteristics, leading to coverage ratios closest to the true values for most of the cases, see Table I while the TLS approach fails to provide a good reconstruction in relative complex situation and also produces some artifacts. Especially in the fifth row (case 5), when the inclusions are located close to each other, the PLS method is still capable of recovering the inclusions reliably, RCR being 1.01, which is an appealing result. Also in Case 7 (Fig. 5), both methods are able to detect the inclusions, although the contrast of the inclusions *w.r.t* the background is much smaller than Cases 1-6. Based on a visual assessment, PLS gives the best reconstruction, leading to a coverage ratio closest to the true value, RCR being 1.09, see Table I.

Note that in the TLS method, the periodical re-initialization of the LSF is necessary to keep it well behaved and to maintain stable evolution, which may cause undesirable results for image reconstruction and add unnecessary computation cost and complexity to the problem [30]. For more detailed reviews of TLS methods in inverse problems, see [25]. Moreover, in PLS reconstruction, we do not employ reinitialization to LSF as in TLS method (e.g., see [19]), and our LSF intrinsically remains well behaved through the corresponding evolution process. Further, we use the identity matrix as the regularization function in PLS, freeing us from the crucial problem of constructing prior covariance (26) as in TLS method. This is major improvement in moving from TLS method to PLS method.

V. SIMULATION STUDIES WITH A THORAX MODEL

To study the performance of the PLS method in medical EIT application: lung imaging, the following two simulation test cases were carried out.

- *Case 8: Lung imaging with homogenous background.* In this test case, the heart was assumed to be in an ideal state, having the same conductivity value as the background, that is, σ_0 is constant.
- *Case 9: Lung imaging with non-homogeneous background.* In real situations, the conductivity of heart is completely different to the background. For this reason, a more realistic value for the heart is assigned, leading to a non-homogenous background. That is, σ_0 is not constant anymore, leading to modeling errors in both PLS and TLS methods, since only one LSF was used in both

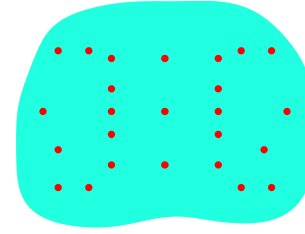


Fig. 6. Distributions of the RBF centers x_i used for the PLS method in the simulation test cases.

methods in the current paper. We note that it is possible to apply two LSFs for representing the regions of lung and heart. However, as our primary interest in this study is to evaluate the performance of the PLS method for lung imaging, we defer this work to the future.

Again, we note that Case 8 where the heart has the same conductivity as the background is not a realistic one. The reason for considering both Case 8 and Case 9 is to study the performance of PLS method with and without modeling errors due to the non-homogenous background.

A. Simulation of EIT Measurements

In both test cases 8 & 9, an actual thorax domain, shown in Fig. 7, was used for simulating the measurements. The thorax domain as well as the sub-domains for the lungs and heart were obtained from CT images of human thorax. The conductivities of the tissues were set as 0.5 mS/cm for lungs, 2 mS/cm for background and 3 mS/cm for heart, corresponding to values found in the literature [42]. Sixteen approximately equally spaced electrodes with length 2 cm were attached on the boundary of the target. The same current injection and measurement patterns used in the previous experimental studies were used in the simulations. The simulated measurements were computed with 2-D FEM approximation using the 2nd order mesh with $N_n = 28101$ nodes and $N_e = 13802$ elements, and the conductivity was approximated by using the 1st order mesh with $N_n = 7150$ nodes. To avoid the so-called ‘inverse crime’, a 2nd mesh with $N_n = 21845$ nodes and $N_e = 10674$ elements was used to compute the voltages, and a 1st order mesh with $N_n = 5586$ for approximating the conductivity in the reconstruction. Note that for each mesh, the number of nodes are different in case of 1st order and 2nd order but elements are same.

To simulate real testing conditions, Gaussian noise with standard deviation 0.1% of the difference between the maximum and minimum value of the noise free measurement data was added to the data V . The selected noise level corresponds to the signal to noise ratio $\text{SNR} = 42\text{dB}$.

B. Implementation Issues

Similarly as in Section IV-B, recall the definition of \mathcal{A} , denoting the mean value of the element area in the FEM mesh. The PLS reconstruction process is initialized with $N = 25$ GRBFs with width parameter variant of $\lambda = \mathcal{K}\mathcal{A}$ placed randomly on the FEM grid in the domain to be imaged. Here, $\mathcal{A} = 0.0773$ and we set again the coefficient $\mathcal{K} = 2$ for both test cases 8&9. A representative image of the distribution of the RBF centers x_i is shown in Fig.6. In the

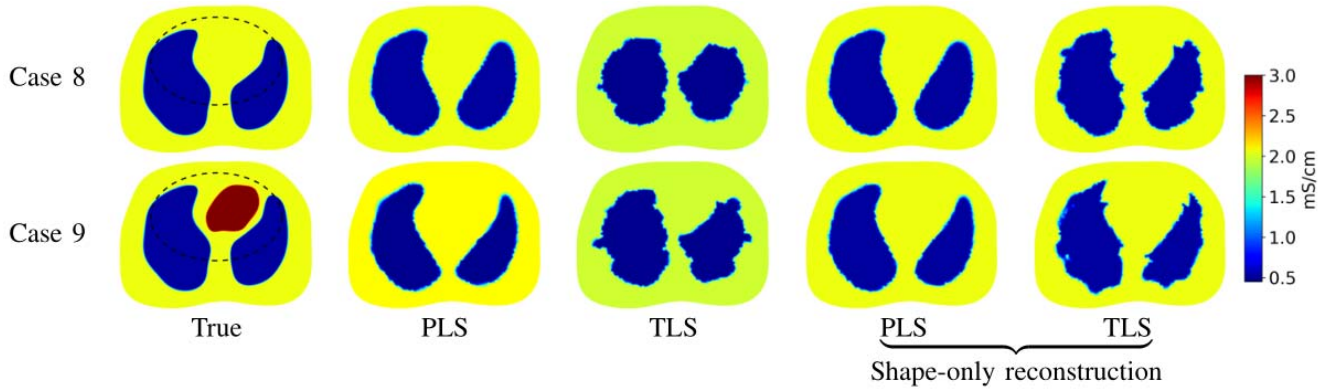


Fig. 7. Reconstructions of cases 8&9. The true simulated conductivity (1st column) and the result of reconstructing both the shape and the binary conductivity values (2nd and 3rd columns), and the shape-only reconstruction (4th and 5th columns) using the PLS and TLS methods. The dashed line shows the cross-section that was used for illustrating the conductivity profiles.

TABLE II

THE RCRs AND SSIM INDEXES OF THE RECOVERED INCLUSIONS AND THE RELATIVE CONTRAST VALUE (RCO) OF THE RECONSTRUCTED σ_j

	Case 8				Case 9				Case 8		Case 9	
	RCR	SSIM	$RCO\sigma_0$	$RCO\sigma_1$	RCR	SSIM [†]	$RCO\sigma_0$	$RCO\sigma_1$	RCR*	SSIM*	RCR*	SSIM* [†]
True	1.00	1.00	1.00	1.00	1.00	1.00	1.00	1.00	1.00	1.00	1.00	1.00
PLS	0.99	0.96	1.00	0.99	0.89	0.91	1.01	0.93	0.99	0.96	0.92	0.93
TLS	0.95	0.80	0.94	0.85	0.99	0.86	0.95	0.86	0.99	0.95	0.91	0.92

* The relative quantities RCR and SSIM marked by asterisk means that the values are based on the shape-only reconstruction with PLS and TLS methods.

† The true image of Case 8 was used as the reference image for computing the SSIM index in Case 9 to avoid the influence arising from the heart region, since our primary interest in this test case is to recover the lung images.

TLS reconstructions, the signed distance function from two given initial circles of radius 6 centered at $(-7, 0)$ and $(7, 0)$, respectively, was applied for the initial LSF.

The initial guess for the binary conductivity values was set to the solution obtained from minimizing the cost function (28), and the resulting $\hat{\sigma}_0$ are 1.7787 mS/cm and 1.7878 mS/cm for Case 8 and Case 9, respectively.

To access quantitatively the recovery of the shape and the binary conductivity values of both PLS and TLS method, we calculated the relative size coverage ratios (RCR), described in Section IV-C, and a relative contrast (RCO)

$$RCO\sigma_j = \frac{\hat{\sigma}_j}{\sigma_j^{\text{True}}}. \quad (29)$$

To allow easy comparison of the values in Table II the relative quantities RCR and RCo were used here instead of the respective quantities CR and $\hat{\sigma}_j$.

For RCo, similarly to RCR, value 1 would indicate exact match of the true and estimated binary conductivity values, while a value greater or less than 1 would indicate overestimation or underestimation, respectively. In addition, we also computed the structural similarity (SSIM) index, see details in [43], for measuring the similarity between the true and reconstructed images.

The reliability of both PLS method and TLS method was also assessed by comparing the reconstructed conductivity distribution profiles, along with a cross section line, to the true profiles in Cases 8&9. The line along which the cross-section is illustrated is marked in the 1st column of Fig.7.

C. Reconstructions Using Simulated Data

The reconstructions of both test Cases 8&9 using the PLS and TLS method are shown in Fig.7. In addition, the shape-only reconstructions with given conductivity values using both methods are also shown.

In Case 8 (the 1st row of Fig.7), when considering the full reconstruction (both the shape and binary conductivity are reconstructed simultaneously), the PLS method provides quantitatively the most accurate reconstructions for the shape of lungs and the binary conductivity σ_j , resulting the best metrics values, see Table II. The TLS method gives a reasonable estimation of σ_j , but fails to provide a complete shape reconstruction and stops further shape enhancement after reaching a local minimum.

With the same problem setting but in less challenging situation of shape only reconstruction (i.e., given the binary conductivity values), the PLS methods performs well in reconstructing shape characteristics, and the reconstruction based on the TLS method is relatively feasible, but with noticeable edge artifacts or serration.

In overall, the PLS method recovers the shape of lungs and the binary conductivity values more accurately, providing superior reconstructions, which is verified by the metrics parameters listed in Table II and the conductivity profiles in Fig.8, the improvement is noticed when compared to the TLS reconstruction. Moreover, when comparing the shape-only reconstructions to the full reconstructions, we found that the PLS method is surprisingly robust *w.r.t* the initialization of σ_j , but the TLS method is very sensitive to the initialization.

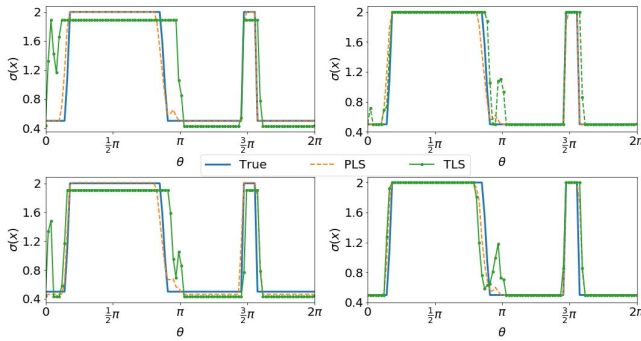


Fig. 8. The true and estimated conductivity distribution profiles. Upper left: The shape and the binary conductivity values were reconstructed for case 8. Upper right: the shape-only reconstruction for case 8. Bottom row: profiles of case 9. Otherwise as in the upper row.

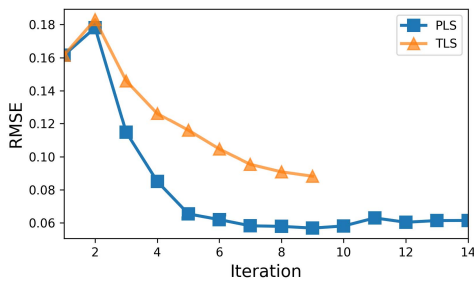


Fig. 9. Root mean square error reduction through the iterative process for full reconstruction (both the shape and binary conductivity are reconstructed) of case 9, using the PLS and TLS methods.

The 2nd row of Fig.7 shows the results of Case 9. The performance of both PLS and TLS methods compared to each other remains similar to the more ideal Case 8; the PLS method gives again successful reconstructions of the shape of lungs and σ_j , leading to the RCo and SSIM index closest to the true value, see Table II. We note that the RCR of PLS is slightly underestimated, which does not go beyond our expectation, due to the modeling errors caused by the non-homogeneous background.

For both test cases, the PLS method does very well in eliminating edge artifacts that were severe when doing TLS reconstructions for the same data set. These effects are also very noticeable in experimental results (Fig. 4), where the edge artifacts were significant.

To compare the convergence behaviors of the PLS and TLS methods, in Fig. 9 we show the root mean square error (RMSE) of the estimated conductivity against the iteration steps for both methods in Case 9. Both reconstructions terminate when there is no further reduction on the cost functions. Apparently, the PLS achieves faster rates of convergence than the TLS method, resulting a smaller RMSE value. In fact, in PLS reconstruction, the updates after 7 iterations become so small that it stops evolving further.

D. Robustness Study of the PLS Method w.r.t Width of the Gaussian Function

To study the performance of the PLS method w.r.t the level of the severity of the Gaussian width parameter, we computed

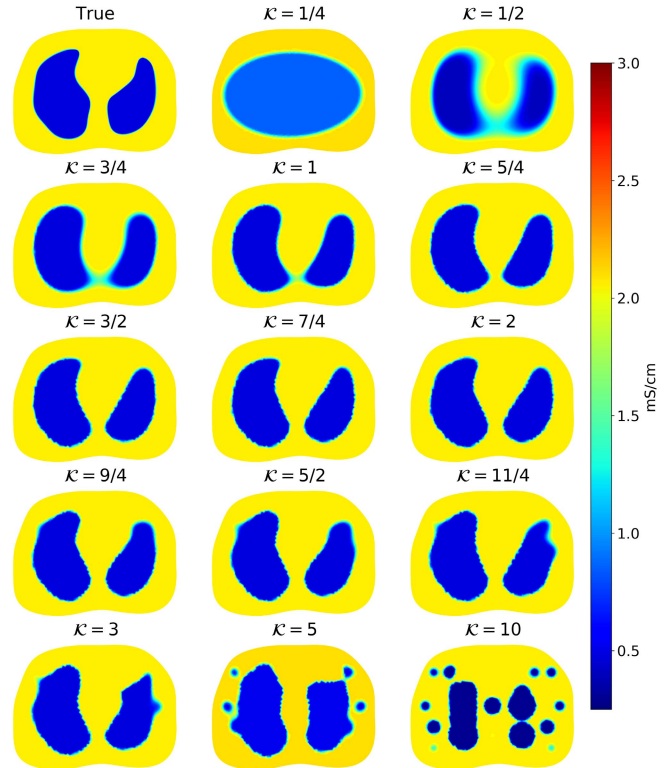


Fig. 10. The result of the robustness study of the PLS method w.r.t the gaussian width coefficient \mathcal{K} selection. The same data set as case 8 was used for reconstructing both the shape and binary conductivity values.

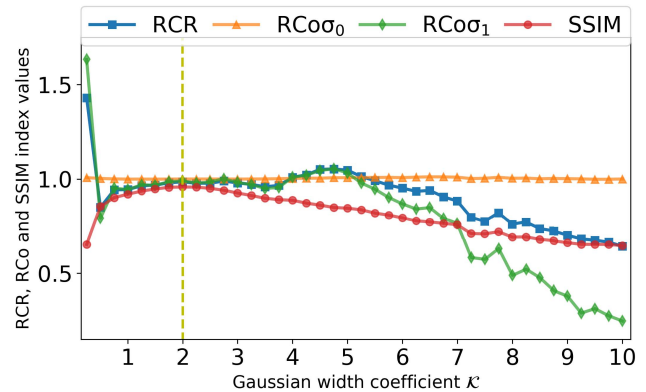


Fig. 11. RCR, RCo and SSIM index versus the gaussian width coefficient \mathcal{K} in case 8 using the PLS method for reconstructing both the shape and binary conductivity values. The dash vertical line denotes the case shown in the 2nd row of Fig. 7.

a set of PLS reconstructions for Case 8 with 40 evenly spaced width coefficients \mathcal{K} in the interval $[1/4, 10]$. Based on (13), (23) and (24), a small coefficient \mathcal{K} means that a large width γ is used, and on the contrary if the coefficient \mathcal{K} is large, a small width γ is applied.

Due to space limitations, we only show the final reconstructions of a subset of this robustness study in Fig.10. The metrics parameters are shown in Fig.11. The effect of different value of \mathcal{K} is well seen in Fig.10, with the smallest $\mathcal{K} = 1/4$, i.e., the largest width γ , PLS fails to produce meaningful result, since a too large width value for RBF will lose the

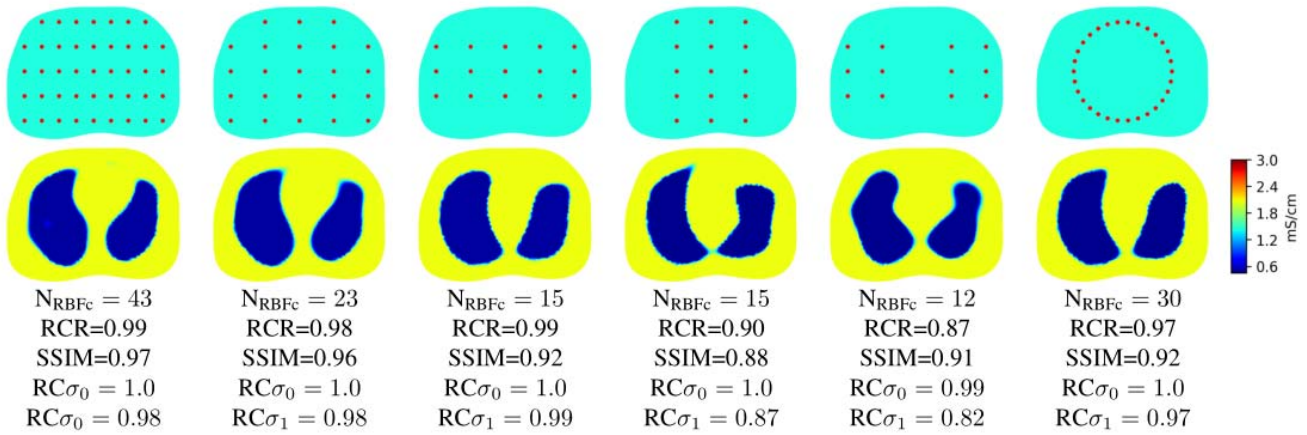


Fig. 12. A study of the robustness of the PLS method to different numbers and centers of RBFs with a fixed $\mathcal{K} = 2$. the same data set as case 8 was applied for estimating both the shape and binary conductivity values.

locality intended for the inclusions in the reconstruction; With the 2nd smallest $\mathcal{K} = 1/2$, blurry image was produced due to the fact that a large Gaussian width determines a large scale of the structures which is smoothed away. On the other hand, a too large values of $\mathcal{K} = 10$ (i.e., too small value of width γ .) results in narrow-band inclusions around the RBF centers. With all the other selected values of \mathcal{K} , the lungs shape and size are well recovered, producing enhanced lung edges, which is verified by the metrics parameters RCR and SSIM indices shown in Fig.11. This trend may reflect sharpening the blurring edge. We note that when the coefficient \mathcal{K} reaches large values 11/4, 3 and 5, the reconstructions contain some edge artifacts or serration, which may related to a trend that reflects producing edge artifacts or serration. In choosing the Gaussian width parameter γ or coefficient \mathcal{K} , one makes a tradeoff between ‘sharpening the blurring edge’ and ‘eliminating edge artifacts’.

In addition, the binary conductivity value σ_0 is accurately estimated for all the selected \mathcal{K} values, while σ_1 is also accurately estimated, except for the estimates corresponding to $\mathcal{K} = [1/4, 1/2]$ and $\mathcal{K} > 11/2$; with those coefficient \mathcal{K} , the conductivity σ_1 is overestimated or underestimated, see Fig.11. It seems that the binary conductivity reconstruction is quite robust to the value of Gaussian width with a proper width coefficient \mathcal{K} tuned between 3/4 and 11/2.

E. Robustness Study of the PLS Method w.r.t RBF Centers x_i

To assess the robustness of the PLS method to different combinations of numbers and locations of RBF centers x_i , we carried out a series of PLS reconstructions for Case 8 with six scenarios (as shown in the 1st row of Fig.12) using the fixed $\mathcal{K} = 2$. The number of RBF centers (N_{RBFc}) was randomly determined and location of x_i was arbitrary selected from a grid over the whole domain Ω . We note there are some other possible strategies for selecting x_i . For example, one alternative way is to start with all the FEM nodes in domain Ω as x_i and then selectively remove centers in a way as to minimize the cost function, which is similar to that used

in RBF network [44], [45]. However, this strategy is rarely practical in EIT applications, as the number of FEM nodes is usually very large.

The results are shown in Fig.12. The top row shows the distributions of x_i and the corresponding estimates based on PLS reconstruction are shown in the middle row, while the bottom row shows the metrics parameters. As can be seen in most cases, PLS reconstruction recovers the lung shape and size. For test case with $N_{\text{RBFc}} = 43$ where the centers roughly equally placed, the PLS reconstruction performs particularly well, producing the best shape estimation of lung and leading to a SSIM closest to the true value, SSIM being 0.97, see Fig. 12. Based on this robustness study, one might conclude that the PLS reconstruction is quite robust to the choice of the initial distribution of RBF centers x_i , given a reasonable choice of N_{RBFc} and equally distributed x_i in the domain to be imaged.

VI. CONCLUSIONS

In this paper, we proposed a PLS method for shape based reconstruction problems in EIT. The proposed method was evaluated by experimental EIT data and two simulated test cases related to EIT imaging of lung. It has been shown that the PLS method provides more accurate estimation of the inclusion shape and the binary conductivity value than the TLS method. The findings demonstrate that the proposed method is not only robust, but also efficient compared to TLS method as it circumvents many difficulties with TLS methods, such as regularization, re-initialization and use of signed distance function. An interesting topic for the future work is to investigate the applicability of the PLS method to more practical problems, e.g., compensation of modeling errors caused by an inaccurately known body shape and electrodes locations in biomedical application of EIT.

ACKNOWLEDGMENT

The authors would like to thank UEF inverse problems group, for providing us with the FEM codes used for the forward solution of the EIT problem and the experimental

data. The authors would also like to thank Antti Voss, MSc, and Gerardo Gonzalez, PhD for the helpful discussions.

REFERENCES

- [1] M. Hallaji, A. Seppänen, and M. Pour-Ghaz, "Electrical impedance tomography-based sensing skin for quantitative imaging of damage in concrete," *Smart Mater. Struct.*, vol. 23, no. 8, p. 085001, 2014.
- [2] M. Wang, Q. Wang, and B. Karki, "Arts of electrical impedance tomographic sensing," *Philos. Trans. Roy. Soc. London A, Math. Phys. Sci.*, vol. 374, no. 2070, p. 20150329, 2016.
- [3] P. Rahmati, M. Soleimani, S. Pulletz, I. Frerichs, and A. Adler, "Level-set-based reconstruction algorithm for EIT lung images: First clinical results," *Physiol. Meas.*, vol. 33, no. 5, p. 739, 2012.
- [4] C. N. L. Herrera, M. F. M. Vallejo, J. L. Mueller, and R. G. Lima, "Direct 2-D reconstructions of conductivity and permittivity from EIT data on a human chest," *IEEE Trans. Med. Imag.*, vol. 34, no. 1, pp. 267–274, Jan. 2015.
- [5] I. Frerichs *et al.*, "Chest electrical impedance tomography examination, data analysis, terminology, clinical use and recommendations: consensus statement of the TRanslational EIT developmeNt stuDY group," *Thorax*, 2016, doi: [10.1136/thoraxjnl-2016-208357](https://doi.org/10.1136/thoraxjnl-2016-208357).
- [6] E. K. Murphy, A. Mahara, and R. J. Halter, "Absolute reconstructions using rotational electrical impedance tomography for breast cancer imaging," *IEEE Trans. Med. Imag.*, vol. 36, no. 4, pp. 892–903, Apr. 2017.
- [7] K. Y. Aristovich, B. C. Packham, H. Koo, G. S. dos Santos, A. McEvoy, and D. S. Holder, "Imaging fast electrical activity in the brain with electrical impedance tomography," *NeuroImage*, vol. 124, pp. 204–213, Aug. 2016.
- [8] V. Kolehmainen, M. Vauhkonen, P. Karjalainen, and J. Kaipio, "Assessment of errors in static electrical impedance tomography with adjacent and trigonometric current patterns," *Physiol. Meas.*, vol. 18, no. 4, p. 289, 1997.
- [9] A. Nissinen, V. P. Kolehmainen, and J. P. Kaipio, "Compensation of modelling errors due to unknown domain boundary in electrical impedance tomography," *IEEE Trans. Med. Imag.*, vol. 30, no. 2, pp. 231–242, Feb. 2011.
- [10] D. Liu, V. Kolehmainen, S. Siltanen, and A. Seppänen, "A nonlinear approach to difference imaging in EIT; assessment of the robustness in the presence of modelling errors," *Inverse Problems*, vol. 31, no. 3, p. 035012, 2015.
- [11] M. Vauhkonen, D. Vadasz, P. A. Karjalainen, E. Somersalo, and J. P. Kaipio, "Tikhonov regularization and prior information in electrical impedance tomography," *IEEE Trans. Med. Imag.*, vol. 17, no. 2, pp. 285–293, Apr. 1998.
- [12] C. R. Vogel, *Computational Methods for Inverse Problems*. Philadelphia, PA, USA: SIAM, 2002.
- [13] B. Schullcke, B. Gong, S. Krueger-Ziolek, M. Soleimani, U. Mueller-Lisse, and K. Moeller, "Structural-functional lung imaging using a combined CT-EIT and a discrete cosine transformation reconstruction method," *Sci. Rep.*, vol. 6, p. 25951, Sep. 2016.
- [14] M. Vauhkonen, J. Kaipio, E. Somersalo, and P. Karjalainen, "Electrical impedance tomography with basis constraints," *Inverse Problems*, vol. 13, no. 2, p. 523, 1997.
- [15] I. Frerichs *et al.*, "Detection of local lung air content by electrical impedance tomography compared with electron beam CT," *J. Appl. Physiol.*, vol. 93, no. 2, pp. 660–666, 2002.
- [16] K. Karhunen, A. Seppänen, A. Lehtikoinen, J. Blunt, J. Kaipio, and J. Monteiro, "Electrical resistance tomography for assessment of cracks in concrete," *ACI Mater. J.*, vol. 107, no. 5, pp. 523–531, 2010.
- [17] E. T. Chung, T. F. Chan, and X.-C. Tai, "Electrical impedance tomography using level set representation and total variational regularization," *J. Comput. Phys.*, vol. 205, no. 1, pp. 357–372, 2005.
- [18] M. Soleimani, O. Dorn, and W. R. B. Lionheart, "A narrow-band level set method applied to EIT in brain for cryosurgery monitoring," *IEEE Trans. Biomed. Eng.*, vol. 53, no. 11, pp. 2257–2264, Nov. 2006.
- [19] M. Soleimani, W. Lionheart, and O. Dorn, "Level set reconstruction of conductivity and permittivity from boundary electrical measurements using experimental data," *Inverse Problems Sci. Eng.*, vol. 14, no. 2, pp. 193–210, 2006.
- [20] D. Liu, A. K. Khambampati, S. Kim, and K. Y. Kim, "Multi-phase flow monitoring with electrical impedance tomography using level set based method," *Nucl. Eng. Des.*, vol. 289, pp. 108–116, Aug. 2015.
- [21] S. Osher and J. A. Sethian, "Fronts propagating with curvature-dependent speed: Algorithms based on Hamilton–Jacobi formulations," *J. Comput. Phys.*, vol. 79, no. 1, pp. 12–49, 1988.
- [22] M. E. Kilmer, E. L. Miller, A. Barbaro, and D. Boas, "Three-dimensional shape-based imaging of absorption perturbation for diffuse optical tomography," *Appl. Opt.*, vol. 42, no. 16, pp. 3129–3144, 2003.
- [23] S. R. Arridge, O. Dorn, V. Kolehmainen, M. Schweiger, and A. Zacharopoulos, "Parameter and structure reconstruction in optical tomography," *J. Phys. Conf. Ser.*, vol. 135, no. 1, p. 012001, 2008.
- [24] F. Larusson, S. Fantini, and E. L. Miller, "Parametric level set reconstruction methods for hyperspectral diffuse optical tomography," *Biomed. Opt. Exp.*, vol. 3, no. 5, pp. 1006–1024, 2012.
- [25] O. Dorn and D. Lesselier, "Level set methods for inverse scattering," *Inverse Problems*, vol. 22, no. 4, p. R67, 2006.
- [26] O.-P. Tossavainen, M. Vauhkonen, L. Heikkinen, and T. Savolainen, "Estimating shapes and free surfaces with electrical impedance tomography," *Meas. Sci. Technol.*, vol. 15, no. 7, p. 1402, 2004.
- [27] G. Barles, H. M. Soner, and P. E. Souganidis, "Front propagation and phase field theory," *SIAM J. Control Opt.*, vol. 31, no. 2, pp. 439–469, 1993.
- [28] J. Gomes and O. Faugeras, "Reconciling distance functions and level sets," *J. Vis. Commun. Image Represent.*, vol. 11, no. 2, pp. 209–223, 2000.
- [29] X. Zeng, L. H. Staib, R. T. Schultz, and J. S. Duncan, "Volumetric layer segmentation using coupled surfaces propagation," in *Proc. IEEE Comput. Soc. Conf. Comput. Vis. Pattern Recognit.*, Jun. 1998, pp. 708–715.
- [30] S. Osher and R. Fedkiw, *Level Set Methods and Dynamic Implicit Surfaces*, vol. 153. New York, NY, USA: Springer, 2006.
- [31] A. Aghasi, M. Kilmer, and E. L. Miller, "Parametric level set methods for inverse problems," *SIAM J. Imag. Sci.*, vol. 4, no. 2, pp. 618–650, 2011.
- [32] M. Hanke, B. Harrach, and N. Hyvönen, "Justification of point electrode models in electrical impedance tomography," *Math. Models Methods Appl. Sci.*, vol. 21, no. 6, pp. 1395–1413, 2011.
- [33] K.-S. Cheng, D. Isaacson, J. C. Newell, and D. G. Gisser, "Electrode models for electric current computed tomography," *IEEE Trans. Biomed. Eng.*, vol. 36, no. 9, pp. 918–924, Sep. 1989.
- [34] E. Somersalo, M. Cheney, and D. Isaacson, "Existence and uniqueness for electrode models for electric current computed tomography," *SIAM J. Appl. Math.*, vol. 52, no. 4, pp. 1023–1040, 1992.
- [35] P. J. Vauhkonen, M. Vauhkonen, T. Savolainen, and J. P. Kaipio, "Three-dimensional electrical impedance tomography based on the complete electrode model," *IEEE Trans. Biomed. Eng.*, vol. 46, no. 9, pp. 1150–1160, Sep. 1999.
- [36] H.-K. Zhao, T. Chan, B. Merriman, and S. Osher, "A variational level set approach to multiphase motion," *J. Comput. Phys.*, vol. 127, no. 1, pp. 179–195, 1996.
- [37] G. Pinggen, M. Waidmann, A. Evgrafov, and K. Maute, "A parametric level-set approach for topology optimization of flow domains," *Struct. Multidisciplinary Optim.*, vol. 41, no. 1, pp. 117–131, 2010.
- [38] D. Liu, V. Kolehmainen, S. Siltanen, A.-M. Laukkanen, and A. Seppänen, "Nonlinear difference imaging approach to three-dimensional electrical impedance tomography in the presence of geometric modeling errors," *IEEE Trans. Biomed. Eng.*, vol. 63, no. 9, pp. 1956–1965, Sep. 2016.
- [39] J. Kourunen, T. Savolainen, A. Lehtikoinen, M. Vauhkonen, and L. Heikkinen, "Suitability of a PXI platform for an electrical impedance tomography system," *Meas. Sci. Technol.*, vol. 20, no. 1, p. 015503, 2009.
- [40] C. Lieberman, K. Willcox, and O. Ghattas, "Parameter and state model reduction for large-scale statistical inverse problems," *SIAM J. Sci. Comput.*, vol. 32, pp. 2523–2542, Sep. 2010.
- [41] A. Lipponen and A. Seppänen, and J. Kaipio, "Electrical impedance tomography imaging with reduced-order model based on proper orthogonal decomposition," *J. Electron. Imag.*, vol. 22, no. 2, p. 023008, 2013.
- [42] C. Gabriel, A. Peyman, and E. H. Grant, "Electrical conductivity of tissue at frequencies below 1 MHz," *Phys. Med. Biol.*, vol. 54, no. 16, p. 4863, 2009.
- [43] Z. Wang, A. C. Bovik, H. R. Sheikh, and E. P. Simoncelli, "Image quality assessment: From error visibility to structural similarity," *IEEE Trans. Image Process.*, vol. 13, no. 4, pp. 600–612, Apr. 2004.
- [44] C. M. Bishop, *Neural Networks for Pattern Recognition*. Oxford, U.K.: Oxford Univ. Press, 1995.
- [45] J. B. Gomm and D. L. Yu, "Selecting radial basis function network centers with recursive orthogonal least squares training," *IEEE Trans. Neural Netw.*, vol. 11, no. 2, pp. 306–314, Mar. 2000.